 doi.org/10.52568/001030/JCSP/44.03.2022

Fabrication of Silica-Tagged Magnetic Nanocatalyst for the Rhodamine-B Dye Degradation from Real Environmental Samples

[1]Abdul Rauf Shaikh, [1]Ghulam Qadir Shar* and [2]Aamna Balouch
[1]*Institute of Chemistry, Shah Abdul Latif University Khairpur Mir's, Sindh, Pakistan.*
[2]*National Center of Excellence in Analytical Chemistry University of Sindh, Jamshoro, 76080 Sindh, Pakistan*
gqadir.shar@salu.edu.pk*

(Received on 10th September 2021, accepted in revised form 9th December 2021)

Summary: This study describes the simple and facile fabrication of silica-tagged magnetic nanostructures (Si@MNs) applied as a nanocatalyst to degrade Rhodamine-B (Rh-B) Dye from the real water samples. Fabricated material has been characterized by using different modern analytical techniques such FT-IR, SEM, XRD, ZS, ZP. According to a morphological study, the fabricated material contains a hexagonal, monoclinic shape and 68 nm in size after successful fabrication and characterization. The catalytic material has been used to degrade the Rh-B Dye. Various parameters have been optimized, such as the effect of reducing agent ($NaBH_4$), impact of dye volume, and influence of catalyst dose to achieve the highest percentage of degradation. At optimal conditions, we get a good percentage of degradation up to 85% having good reproducibility. Fabricated catalyst has been successfully applied for actual water samples.

Keywords; Silicon tagged magnetic nanostructures; Rhodamine-B dye; Catalytic activity; Removal.

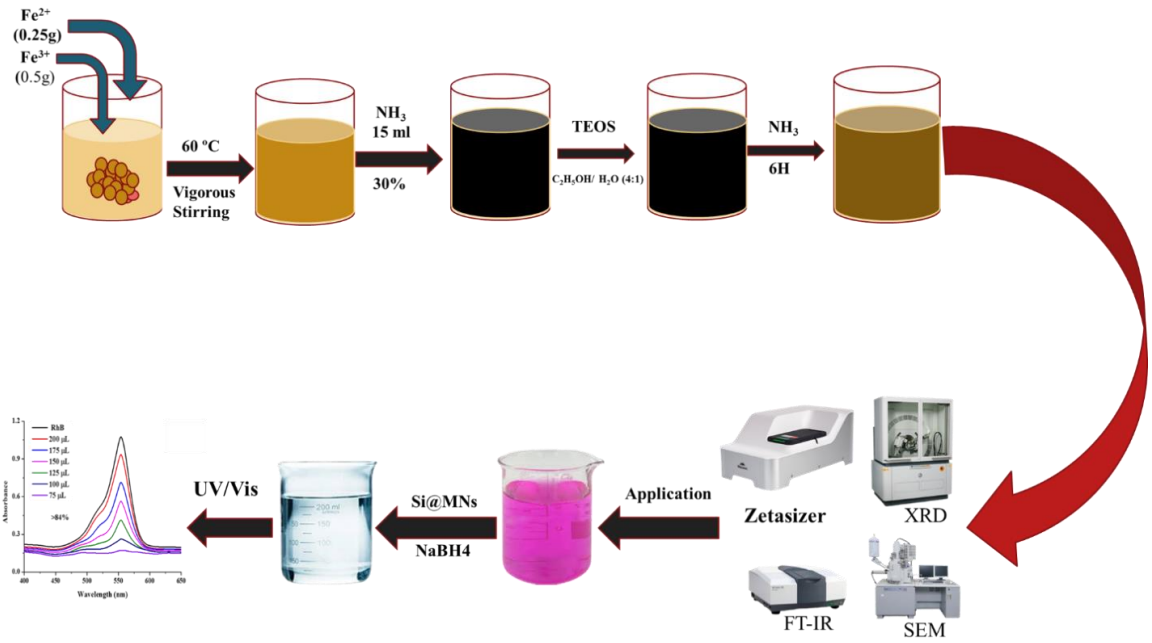

Graphical representation of Si@MNs synthesis and application

Introduction

Organic dyes are coloring compounds used in fabric, leather, and cosmetics products in different industries. The huge utilization of dyes and hazardous dumping cause critical natural concerns [1]. The organic dyes usually have a complex aromatic arrangement with anionic, cationic, and covalent characteristics. Organic dye pollution is becoming a problem owing to non-ionic properties of non-ionic dyes such as rhodamine B (Rh-B), crystal violet (CV), methylene blue (MB), methyl orange (MO), Congo red (CR), and Remazol Black-B (RB5) [2, 3]. The color of organic dyes can be detected even at low concentrations. Dyes are insoluble in water and risky to the environment and human health [4]. More than ten thousand different pigments and organic dyes with an annual production of more than 07 million tons

commercially occur. More than 5% of organic dyes material is dumped as an industrial discharge[5]. Rhodamine B (C28H31N2O3Cl, MW = 479 g/mol) is a xanthene dye with the IUPAC designation[9-(2-carboxyphenyl)-6-diethylamino-3-xanthenylidene]-dimethylammonium chloride The λ -Max of rhodamine B dye is 553 nm [6, 7]. The dye is neurotoxic and carcinogenic to humans and aquatic life; it also causes shortness of breath, irritation of the eyes, skin, vomiting, gastrointestinal tract, chest discomfort, coughing, respiratory tract, and the ability to grow ambiguous tumors [8, 9]. Because RhB inhabits the light penetration, it also reduces the process of photosynthesis. In Biochemical investigations, Rhodamine B is widely used as a colorant in the textile industry, as a forbidden food preservative, and as pigments [10]. RhB dye is widely used in biotechnology applications such as flow cytometry, fluorescence microscopy, fluorescence correlation spectroscopy, and enzyme-linked immunosorbent assay (ELISA) [11]. Due to the pink color, the RhB has been widely used in different industrial products such as textile, cosmetics, food, and drug. RhB is also used as a tool for tracking water pollution. On the industrial scale, the RhB is primarily unsafely dumped. It causes some toxic effects on human health and the environment. Rhodamine B dye is now restricted as a food coloring since it is a harmful material [12]. It may cause a long-term poisonous impact on the water system, and it is very harmful when it comes into contact with the skin. On the other hand, RhB may cause cancer and congenital diseases. Due to the toxic effects on human health, different countries have prohibited the use of RhB in food [13, 14]. Due to its poisonous effects, researchers used other methods, including precipitation, membrane filtration, flocculation, photocatalytic degradation, and adsorption [11]. Still, reported methods have limitations such as time consumption, pH limitations, and cost-effectiveness. The researcher focuses on new nanoparticle materials for the catalytic degradation of dyes from wastewater to overcome these limitations. Because water is a vital component of all living organisms, life would be impossible without it. On average, living organisms have 70 to 90% water in their bodies. It is impossible to conceive of living without clean water. One of today's biggest social, technological, economic, and political challenges is the decline in freshwater quantity and quality. The world's population grows, so does the need for safe drinking water. Without a doubt, no raw element in the world is more valuable than water. The addition of some undesired components from various sources, such as agricultural and industrial effluents, may cause water pollution [15]. One of the major sources of water pollution is the textile sector. Dyeing and preparing cloth in the textile industry demands a considerable quantity of water and is regarded as a major water consumer and the largest dye consumer sector; nearly the whole textile industry utilizes over 10,000 different Dyes. The textile industry's effluents contain a significant proportion of dyestuff, often a complex organic substance [16]. Two typical approaches to preparing nanomaterials are used: (1) top-down nano-synthesis and (2) bottom-up nano-synthesis [17]. In the first example, enormous structures are formed by successive cuts, but in the second situation, nanostructures are created by individual atoms or molecules. As a result, the properties of nano-scale materials have changed. They now exhibit newly enhanced and innovative physical, chemical, and biological properties based on their specific size, shape, morphology, distribution, and surface-to-volume ratio compared to macro-sized materials. Nanotechnology has attracted researchers due to its wide applications ranging from packing and textile to catalysis and semiconductor [18]. The surface to volume ratio of nanoparticles enhances the reactivity, optical and electrical properties. However, magnetic nanoparticles, particularly iron oxide, possess multiple technological applications, including biomedicine, engineering, and industrial [19, 20]. Certain oxides of iron (such as hematite, Fe2O3, magnetite, and Fe3O4) possess magnetic susceptibility and other unique properties (catalytic, photoactive, and mechanical), due to which can be utilized in a variety of applications in the field of energy harvesting, environmental bioremediation, catalysis, magnetic resonance imaging contrast agents, magnetic separation and cell sorting [21, 22]. Hematite is a well-known iron oxide that exhibits modest ferromagnetic or antiferromagnetic activity at ambient temperature, however, it is paramagnetic at 956 K. The magnetic properties of these polymorphs are related to their structures, size, and shape; therefore, α-Fe2O3 is canted antiferromagnetic, β-Fe2O3 is paramagnetic, and γ-Fe2O3 and ε-Fe2O3 are ferromagnetic. They concluded that the small NPs show superparamagnetic behavior and exhibit a high exchange bias field. Size morphology also affects the magnetic behavior of IONPs. One-dimensional (1D) IONPs exhibit different magnetic properties compared to higher dimensional particles. A recent study revealed that the magnetic properties of single and tubular clustered IONPs varied as a function of morphology [23, 24]. Hematite (α-Fe_2O_3) and Maghemite (γ-Fe_2O_3) are well-known iron oxide phases among magnetic nanoparticles due to their magnetic properties, chemical stability, and nontoxicity. They have gained acceptance in several fields of application of nanomaterials such as magnetic recording systems, magnetic refrigeration, magneto-optical devices,

magnetic resonance imaging, magnetic separation techniques, and separation and purification of biological molecules. Iron oxide nanoparticles are polymeric, including different hydroxides, oxides, and oxy-hydroxide. Most of them contain trivalent iron, such as hematite (α-Fe_2O_3), the more stable form of iron found in nature, and ferrihydrite ($Fe_5HO_8 \cdot {}_4H_2O$) [25]. The hexagonal unit cell of α-Fe_2O_3 is characterized by two-thirds of the octahedral sites being filled by Fe^{3+} ions (corundum structure). It contains an n-type semiconductor with an Eg of 2.1 eV. It has been employed in a variety of applications because it is a readily accessible, ecologically benign, and non-toxic substance that is seldom impacted by oxidation changes [26, 27]. The hematite nanoparticles are highly stable, have low toxicity, high surface-to-volume ratio, and have unique properties.

Due to its novel properties, hematite is ideal for many applications in emerging fields. In particular, the hematite nanoparticles have been used in cheaper and greener photocatalysts for water oxidation and use for artificial photosynthesis, gas sensors, pigments, lithium-ion batteries, magnetism, biomedical applications, and electrochemical capacitors [28- 34]. The present study describes the simple and facile fabrication of silica tagged magnetic nanostructures (Si@MNs) applied as a nanocatalyst to degrade Rh-B dye from the real water samples. Fabricated Si@MNs have been characterized using different modern techniques such FT-IR, SEM, XRD, ZS, ZP. The Si@MNs have been used to degrade Rhodamine-B dye; other parameters have been optimized, such as the effect of reducing agent, the impact of dye volume, and the influence of catalyst dose to obtain a maximum percentage of degradation. We get sound percentage degradation up to 85% at optimal conditions having good reproducibility. Fabricated Si@MNs have been successfully applied to natural water.

Material and Methods

Chemicals

All the chemicals and reagents of analytical grade were used throughout this study, such as ferric chloride ($FeCl_3$), ferrous chloride ($FeCl_2.4H_2O$), sodium chloride, Sodium borohydride, ammonium hydroxide (33%). Rhodamine B was obtained from Merck AG (Darmstadt, Germany). Mili-Q water has been used during the whole experiment study, including preparing the stock solution.

Experimental

Preparation of Iron Oxide nanoparticles

Iron oxide nanoparticles were prepared by a modified co-precipitation method [35, 36]. The 0.5g of Ferric Chloride and 0.25g of ferrous chloride were separately dissolved in a beaker. Then the solution was transferred into the reaction flask then homogenized the solution under the vigorous mechanical starrier at 60 °C. After that, a 15ml of 33% NH_3 solution was added dropwise to the solution. The color of the solution changed from golden to black, indicating the formation of magnetic nanoparticles. It was confirmed using the external magnetic field. The resulting precipitates were washed with deionized water and ethanol three times. A solution of 0.5 g NaCl in 100ml deionized water was added to neutralize the prepared particles. Finally, the synthesized particles were dried at 80°C.

Synthesis α -Fe_2O_3 into the silica

The MNs were synthesized using 0.5g of MNs into the reaction flask, and 100ml of the solvent mixture contained a ¼ ratio of water and ethanol. The mixture was vigorously stirred with a mechanical starrier. When the particles were dispersed, 10ml of ammonia solution, 33% were added. After that, 5ml of TEOS were added. The reaction proceeded at room temperature for up to 8 hours. The mixture was centrifuged to collect catalyst washed several times with deionized water and ethanol. Finally, the obtained catalyst was dried and collected.

Characterization Techniques

The Fourier Transform Infrared spectrometer model (Thermo Nicolet 5700) was used to study the functional group present in the silica tagged magnetic nanoparticles Si@MNPs ranging from 4000 to 500cm-1. Scanning Electron Microscope (SEM) was used to study the engineered nanostructure model's surface morphology and physical texture (JSM 6380 Joel, Japan). X-ray Diffraction 183 (XRD) was used to investigate phase purity. The crystalline nature of the synthesized Si@MNPs was checked using a model (XRD, Bruker D8) UV–visible spectrophotometer (Biochrom Libra S22) to analyze rhodamine B λ-max at 553 nm. X-ray photoelectron spectroscopy (XPS) was used to analyze the shell structure. Zeta Sizer was used to measure the size and zeta-potential. Zeta Potential tests were conducted using Laser Doppler Velocimetry (LDV) technique by Malvern Zeta Sizer Nano-ZS. We studied the surface charge properties of the nanoparticles of Fe-oxides and investigated a possible correlation between morphologies of nanoparticles (shape and size).

Results and Discussions

FTIR study

FTIR study was carried out to check the interaction of functional material with MNPs. Fig.1 shows the two spectra; one is Fe_2O_3, and the second is Fe_2O_3@SiO_2. FTIR spectrum is around 577 and 631 cm−1, which confirms the existence of Fe-O nanoparticles, as shown in Fig.2. The massive absorption peak is based at 3431 cm−1 and highest at 1631 cm−1 and is attributed to the stretching and bending motions of the OH groups and H2O molecules [37]. The distribution shows a limited volume of dissolved H2O on the surface of the substance and intrinsic OH groups on the same level as the preparations. The peak at 1091.0 $cm^{-1}$is assigned to the Si-O-Si peak from the silanol group beside these two shoulder peaks at 778.8 and 470.2 cm^{-1} corresponds to Si-O-H and Si-O bonds vibration, respectively. This indicated the successful fabrication of the silica layer on the magnetic nanoparticles [38].

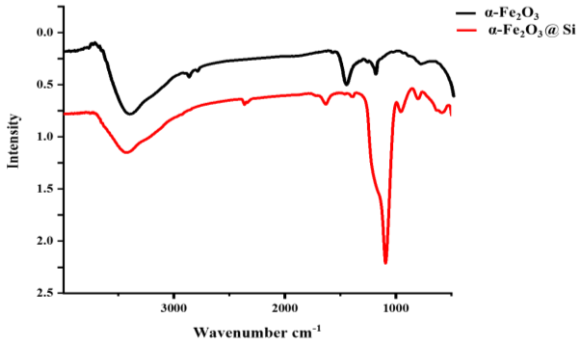

Fig. 1: FTIR spectrum of the nanoparticle Si@MNs.

SEM study

The morphological study was carried out by using the SEM. The scanning electron microscopy examination findings clearly reveal in Fig.2 that the silica doped iron nanostructures are in the shape of nanotubes, clearly demonstrating that the monoclinic types of nanotubes contain hexagonal cross fragments with a length of 68 nanometers. This size is conformed to the zeta sizer. The nanotubes have shown a new way to produce novel nanostructures of silicon that can hold promise for silicon-based nanodevices from a technological point of view. Such materials are exciting and used in different sensors, electronics, and catalysis. The encapsulation of metals in the silicon enhances the stability, and strong selectivity and controls the size of synthesized materials.

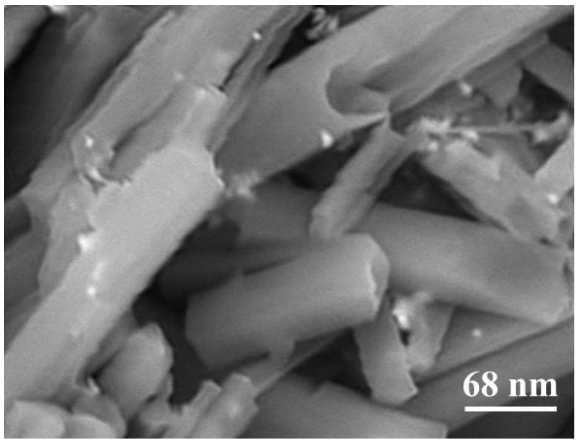

Fig. 2: SEM nanoparticle Si@MNs.

XRD analysis

X-ray diffraction is a prevailing technique for material characterization because it provides valuable information about the inner structure of particles, such as sample nature (crystalline/amorphous), crystallite size, and crystal structure. The crystal structures of this nanostructure were explored. The XRD analysis shows that these nanostructures are hematite (α-Fe_2O_3); as Fig.3 shows, the peaks attributed to nanostructures' XRD pattern correspond to the α-Fe_2O_3 hexagonal process. The XRD spectrum of the nanostructures contains nine distinguishable peaks. The peaks appearing at a 2θ range of 24.18 °, 33.16 °, 35.63 °, 40.61 °, 49.48 °, 54.08 °, 57.42 °, 62.46 °, and 64.15 ° may be associated with crystalline structures of 012, 104, 110, 113, 024, 116, 018, (214) and (300) corresponding to pure nanostructures of α-Fe_2O_3. The most intense peak was observed at 2θ = 32.67°, indicating that the hematite materials obtained are exceptionally crystalline [39, 40]. Peak and intensity positions were in good agreement with reported values. JCPDS No.89-5899 confirmed the phase structure of hematite (α-Fe2O3).

XPS study

The XPS technique was used to analyze Fe's shell structure and oxidation state in α-Fe_2O_3. Fig.4 displays descriptive XPS spectra of the hematite. A typical survey scans the spectrum from 0 to 1000 eV of the Fe_2O_3, showing cores rates, such as Fe 2p, O 1s, and satellite peaks. Only the peaks due to iron, oxygen, and carbon are observed. The peak positions corresponding to Fe 2p and O 1s have been checked in the bond energy range 730–742 and 531–532 eV. At 531 eV, O1s oxygen peak was observed. It is well known that oxygen takes two chemical states due to O_2−& O− 2having lower and higher bond energy, respectively. The peaks at (531 eV) and 532 eV can be attributed to the chemical bonded –OH group on the surface of α-Fe_2O_3. Elemental review

verified Fe, C, and O necessary signatures. In the XPS spectra, there were no more elementary signals found. In addition, the O1s core level spectrum displays the Powerful oxide peaks at about 531 eV, which are in solid contrast with the literature data on α-Fe_2O_3 [41]. Fe 2p and O 1s core levels suggest that Fe and O valence states are +3 and 2, respectively. Consequently, when this finding is combined with that of XRD, it can be inferred that the substance is pure α-Fe_2O_3, and no other impurities, such as Fe_3O_4, are present.

Zeta Sizer (ZS) study

The particle size distribution of NPs was obtained by dynamic light scattering using Zeta Sizer to measure the size and zeta-potential to maximize stability and life span and accelerate the production of formulations. In the backscattering mode (angle of detection 173°, measuring position 1 mm from the cuvette wall), the instrument detects the time development of the intensity of light scattered by moving particles in the sample after irradiation with a He-Ne laser beam. The auto tiltrotor is used to optimize pH titrations and calculations. The nanoparticle size distributions were small, while the average diameter of the particles was 68 nm, estimated by MALVERN ZETA SIZER, as shown in Fig.5 [42]. The data shown in this work represent the mean distributions calculated from four independent repetitions. The measurement was carried out at laboratory temperature.

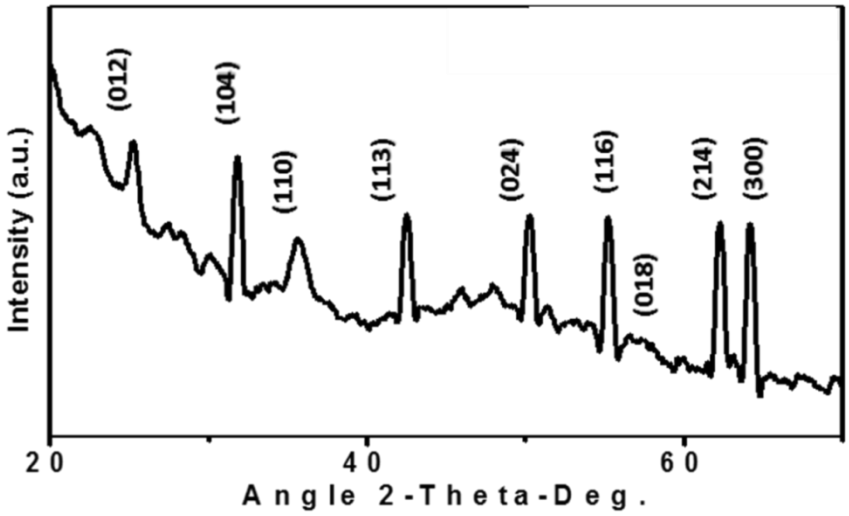

Fig. 3: XRD pattern of the Si@MNs nanoparticle.

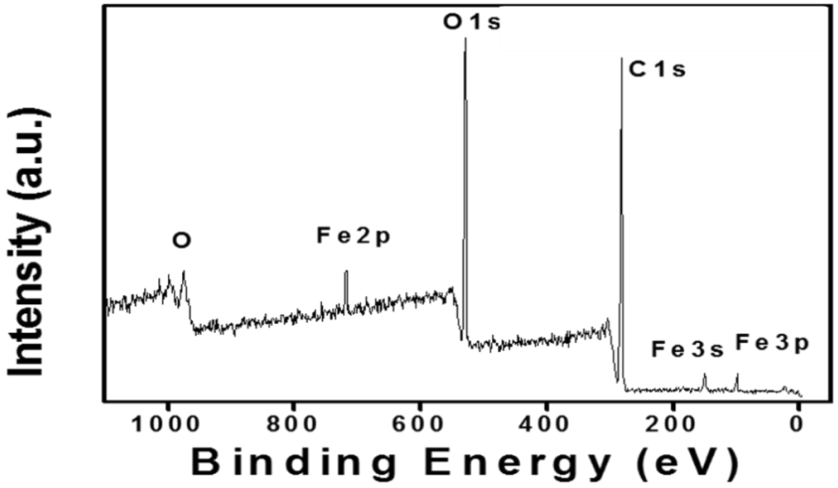

Fig. 4: X- XPS Spectrum of Si@MNs structures.

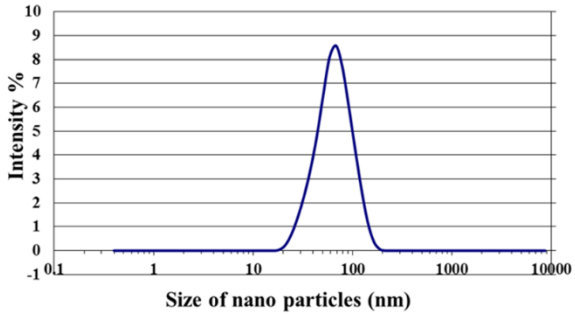

Fig. 5: Zeta sizer of Synthesis Si@MNs.

Zeta Potential (ZP) study

Zeta Potential tests were conducted using Laser Doppler Velocimetry (LDV) technique by Malvern Zeta Sizer Nano-ZS. We studied the surface charge properties of the nanoparticles of Fe-oxides. We investigated a possible correlation between morphologies of nanoparticles (shape and size) and surface charge at the dropping plane. This type of correlation is commonly used to study the physicochemical stability and biomolecular interaction with nanoparticles. When there is potential in the range of + 30 to -30 millivolts, the particle is stable. The pH values observed in the corresponding suspensions were noticed to fall in the 6.5–5.5 range. A sudden shift in zeta potential, from positive to negative values, was observed in this small pH period. The surprising aspect concerns the negative charge at this pH interval (average pH 6) of most of the hematite samples investigated. Only positively charged particles are predicted to be identified as the point of zero charges (ZPC) for the hematite. At the same time, most of the iron oxide surface charge investigations were conducted by varying the ionic strength and pH [43]. The stability of the IONPs was proved to be good as the zeta potential existed in the -23 mv range, as shown in Fig. 6.

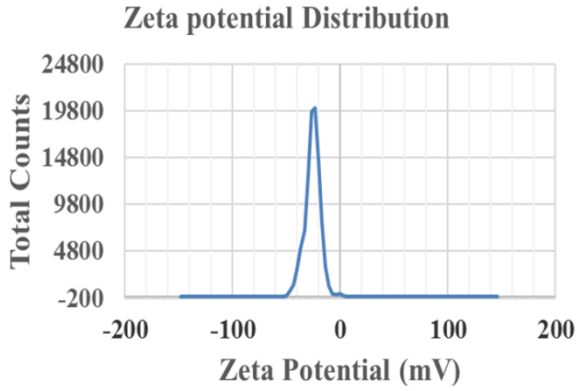

Fig. 6: Zeta Potential of Synthesis Si@MNs.

Catalytic performance during the degradation of Rh-B

Nano-catalytic-based degradation of Rhodamine B dye was done using Si@MNS with the addition of NaBH4. The degradation study was carried out in the presence and absence of catalyst and NaBH4. The characteristic peak of Rh-B was observed at 553 during the UV analysis. In the initial stages, as Fig. 7 shows, when the nanocatalyst was added to the standard solution of Rh-B, the color of the solution disappeared, and the peak intensity decreased. It is due to the reduction of Rh-B in the presence of Si@MNS.

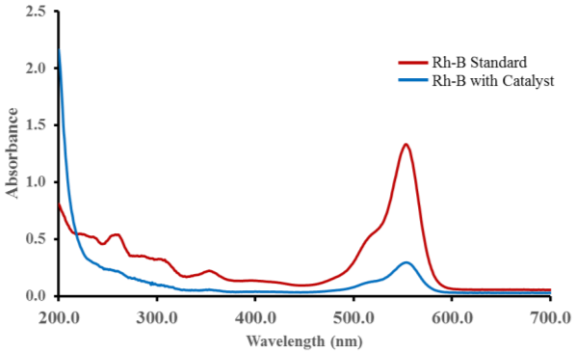

Fig. 7: UV result of the catalytic effect on the Rh-B.

Impact of reducing agent ($NaBH_4$) on the degradation of Rh-B

The $NaBH_4$ is a crucial factor; it plays a significant role in producing the proton source during Rh-B dye degradation. The volume of $NaBH_4$ (0.2M) was optimized from 25 µL to 125 µL to check the effect of $NaBH_4$ on the reduction of Rh-B dye. Fig. 8 showed when the volume of the reducing agent was increased, the percentage of degradation also increased up to 100 µL. After that, no significant change was observed. Thus, 100 µL was optimal for further study.

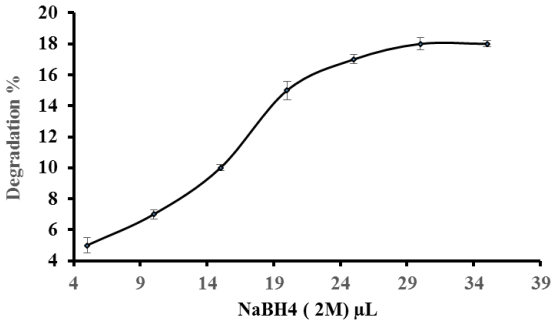

Fig. 8: Effect of reducing agent.

Effect of catalyst dose

The amount of catalyst plays a vital role in the degradation of Rh-B. The dose study was carried out in the range of 0.15mg-0.25 mg. Fig. 9 shows that when the amount of the dose increases, the disappearance of the color of Rh-B also increases, and UV/Vis spectra intensity of peak also decreases. The rise in the conversion of Rh-B dye with increasing the amount of catalyst could be attributed to the increase in the active catalytic sites required for dye reaction. This can be explained in the following way. As the volume of the catalyst increases, the number of dye molecules adsorbed to the catalyst surface increases. Because of this high surface molecular density, the rate of dye removal increases. The decrease in Rh-B dye degradation with the rise in catalyst quantity is attributed to the increase in turbidity of the suspension [44]. Deactivation of activated molecules of dye by collision with a higher catalyst loading influences the reaction. Due to this high surface molecular density, the dye degradation rate increases. The decline in degradation of Rh-B dye with a raise in catalyst volumes is the decrease in Rh-B dye degradation with a raise in catalyst amounts is attributed to turbidity rises of the suspension deactivation of activated molecules of dye by collision with a higher catalyst loading influence the reaction. Thus the degradation rate is decreased at a higher amount of catalyst [45].

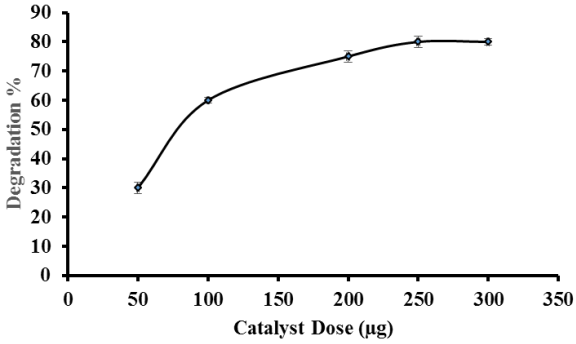

Fig. 9**:** Effect of catalyst dose

Effect of Dye Volume on Degradation

The prepared Si@MNPs nanostructures were used as a heterogeneous catalyst for the degradation of Rh-B dyes. When $NaBH_4$ is added, the aqueous solution of Rh-B shows an intense peak at 554 nm. The reactions to the reduction were calculated from the substantial decrease in absorbance, which was evaluated as a function of time. The red-colored mixture became colorless on complete reduction of the dye, corresponding to the azo bond cleavage and colorless amino compounds. Different initial volumes of 75, 100, 125,150,175, and 200uL were tested to determine the effects of dye volume on Rh-B dye degradation. We performed experiments using 250ug of Fe_2O_3 /$SiO_2$of (0.01M) Rh-B dyeing solutions at 650 rpm, and samples from the dye mixture were regularly examined after 1, 2, 3,4,5, and 6 minutes. For each sample, the UV-visible spectrum was recorded. The absorbance of Rh-B for all samples was found at λ -Max 554 nm. This was mentioned that approximately 84, 72, 66, 56, 48, and 36 percent of 75,100,125,150,175 & 200 uL degraded during the first six minutes. The deterioration increased steadily to 84, 72, 66, 56, 48, 42, and 36% after 8 minutes of reaction time, respectively. It was noted that degradation by percentage decreases with increasing dye volume using Fe_2O_3/SiO_2 (0.01M) as a constant for all dye volumes. At 75uL 84% dye degradation was optimized [46, 47]. Fig.10a shows the UV/Vis results of degradation and Fig. 10 graphical view percentage of degradation.

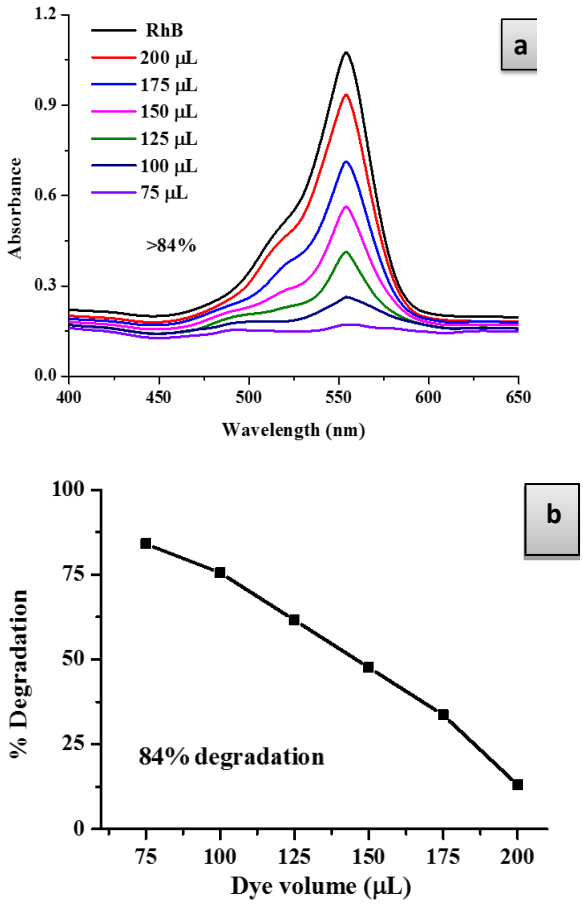

Fig. 10: (a) shows the UV/Vis degradation results and (b) Graphical view degradation percentage.

Table-1: Represents the comparative study.

Catalyst	Dye	Accelerator	%Degradation	Time(min)	Reference
NiO	Rh-B	$NaBH_4$	76	30	[29]
CuO petals	Rh-B	H_2O_2	80	300	[30]
N-CuO NS	Rh-B	H_2O_2	80	180	[31]
CuO flowers	Rh-B	H_2O_2	80	300	[31]
C-CuO NS	Rh-B	H_2O_2	80	60	[31]
$H_3PW12O40/SiO_2$	Rh-B	H_2O_2	85	120	[32]
Si@MNs	Rh-B	$NaBH_4$	85	1.30	Present study

Reusability

Reusability is crucial to show that the fabricated material is economical or environmentally friendly. We checked the reusability of silica-tagged magnetic nano-structures Si@MNs under the optimal conditions. Fig.11 shows the reusability of Si@MNs nanocatalyst that the degradation percentage decreases up to 4% from one cycle to six cycles. It indicates that Si@MNs nanocatalyst economical is beneficial, cheaper, and greener.

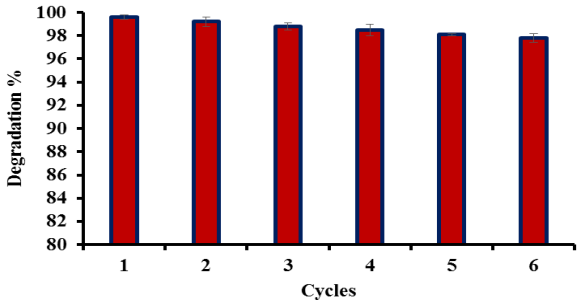

Fig. 11: Reusability study of Si@MNs.

Comparative Study

The proposed method has been compared with the reported method. The Si@MNs have good catalytic efficiency, low time consumption, and a good degradation percentage compared to the reported procedure given in the Table-1 Hence, it is a confirmation that fabricated material is highly efficient and environmentally nanocatalyst.

Conclusion

This study aims to prepare an efficient, economical, and environment-friendly nanocatalyst for wastewater treatment. The silica tagged nanostructure was successfully synthesized using the co-precipitation route. The surface morphology and crystal characteristic, size distribution, and the surface potential of prepared material were analyzed via powered SEM, XRD, and zeta sizer, respectively. The catalytic efficiency of silica-tagged magnetic nanostructures was studied against Rh-B dye solution using $NaBH_4$ as a reductant. The nanocatalyst has shown high stability with a huge surface-to-volume proportion that provides an excellent platform for the catalytic efficiency towards the Rh-B dye degradation. The excellent catalytic performance is due to the high number of dynamic sites, which enables nanostructure characteristics compared to other catalytic materials reported to date. The experimental results of Si@MNs are excellent in words the Rh-B dye degradation.

Acknowledgments

The authors gratefully acknowledge Dr. Muhammad Saqaf Jagirani that supports writing a research paper and experimental work. The authors gratefully acknowledge the NCEAC Laboratory, University of Sindh, Pakistan, for providing the facilities to perform the research work.

References

1. S. Haider, A. Haider, A. Ahmad, S.U.-D. Khan, W.A. Almasry, M. Sarfaraz, Electrospun Nanofibers affinity membranes for water hazards remediation, *Nano. Res. J.*, **8,** 511 (2015).
2. S.A. Yasin, J.A. Abbas, I.A. Saeed, I.H. Ahmed, The application of green synthesis of metal oxide nanoparticles embedded in polyethylene terephthalate nanofibers in the study of the photocatalytic degradation of methylene blue, *Polym. Bull.*, **77,** 3473 (2020).
3. A.S.H. Makhlouf, A. Barhoum, Fundamentals of nanoparticles: classifications, synthesis methods, properties and characterization, *William, Andrew*, p.233 (2018).
4. A. Mohamed, R. El-Sayed, T. Osman, M. Toprak, M. Muhammed, A. Uheida, Composite nanofibers for highly efficient photocatalytic degradation of organic dyes from contaminated water, *Environ. Res.*, **145,** 18 (2016).
5. I. Acar, A. Bal, G. Güçlü, Adsorption of Basic Dyes from Aqueous Solutions by Depolymerization Products of Post-Consumer PET Bottles, *Clean–Soil, Air, Water*, **40,** 325 (2012).
6. J. Singh, T. Dutta, K.H. Kim, M. Rawat, P. Samddar, and P. Kumar, Green'synthesis of metals and their oxide nanoparticles: applications for environmental remediation, *J. nanobiotechnology*, **16**, 1 (2018).

7. C. Lops, A. Ancona, K. D. Cesare, B. Dumontel, N. Garino, G. Canavese, S. Hérnandez, and V. Cauda, Sonophotocatalytic degradation mechanisms of Rhodamine B dye via radicals generation by micro-and nano-particles of ZnO, *Applied Catalysis B: Environ.,* **243**, 629 (2019).
8. S. S. Imam, and P. Panneerselvam, Enhanced rhodamine B dye adsorption by groundnut shell activated carbon coated with Fe3O4, *Elixir Applied Chem.,* **86,** 34984 (2015).
9. S. Ramanathan, S. P. Selvin, A. Obadiah, A. Durairaj, P. Santhoshkumar, S. Lydia, S. Ramasundaram, and S. Vasanthkumar, Synthesis of reduced graphene oxide/ZnO nanocomposites using grape fruit extract and Eichhornia crassipes leaf extract and a comparative study of their photocatalytic property in degrading Rhodamine B dye, *J. Environ. Health Sci. and Engr.,* **17**, 195 (2019).
10. K. Kaviyarasu, C. M. Magdalane, D. Jayakumar, Y. Samson, A. K. H. Bashir, M. Maaza, D. Letsholathebe, A. H. Mahmoud, and J. Kennedy. High performance of pyrochlore like Sm2Ti2O7 heterojunction photocatalyst for efficient degradation of rhodamine-B dye with waste water under visible light irradiation, *J. King Saud Uni.Sci.,* **32**, 1516 (2020).
11. J. Wu, X. J. Zhang, K.-Q. Shi, Y.-P. Chen, Y.-F. Ren, Y. J. Song, G. Li, Y. F. Xue, Y. X. Fang, Z. J. Deng, and X. Xu. Hepatitis B surface antigen inhibits MICA and MICB expression via induction of cellular miRNAs in hepatocellular carcinoma cells, *Carcinogenesis*, **35,** 155 (2014).
12. M. D . C. Cotto-Maldonado , T. Campo, E. Elizalde, A. G. Martínez, C. Morant, and F. Márquez, Photocatalytic degradation of rhodamine-B under UV-visible light irradiation using different nanostructured catalysts, *Chem. Sci. Int. J.*, **3,** 178 (2013).
13. M. Soylak, Y.E. Unsal, E. Yilmaz, M. Tuzen, Determination of rhodamine B in soft drink, waste water and lipstick samples after solid phase extraction, *Food Chem. Toxicol.*, **49,** 1796 (2011).
14. N. Pourreza, S. Rastegarzadeh, A. Larki, Micelle-mediated cloud point extraction and spectrophotometric determination of rhodamine B using Triton X-100, *Talanta*, **77,** 733 (2008)..
15. A. A. Jahagirdar, M. Z. Ahmed, N. Donappa, H. Nagabhushana, and B. M. Nagabhushana, Photocatalytic degradation of rhodamine B using nanocrystalline α-Fe2O3, *J. Mater. Environ. Sci.*, **5**, 1426 (2014).
16. M. Saeed, M. Ilyas, and M. Siddique, Kinetics of lab prepared manganese oxide catalyzed oxidation of benzyl alcohol in the liquid phase, *Int. J. Chem. Kinetics*, **47**, 447 (2015).
17. N. D. Jaji, H. L. Lee, M. H. Hussin, H. M. Akil, M. R. Zakaria, and M. B. H. Othman, Advanced nickel nanoparticles technology: From synthesis to applications, *Nanotechnology Reviews*, **9**, 1456 (2020).
18. S. K. Maji, N. Mukherjee, A. Mondal, B. Adhikary, Synthesis, characterization and photocatalytic activity of α-Fe_2O_3 nanoparticles, *Polyhedron*, **33,** 145 (2012).
19. M. Pardavi-Horvath, Microwave applications of soft ferrites, *Magn. Magn. Mater.*, **215,** 171 (2000).
20. R. M. Cornell, U. Schwertmann, The iron oxides: structure, properties, reactions, occurrences and uses, *John Wiley & Sons*, p.1 (2003).
21. W. Wu, Z. Wu, T. Yu, C. Jiang, and W.S. Kim, Recent progress on magnetic iron oxide nanoparticles: synthesis, surface functional strategies and biomedical applications, *Sci. and techno. adva. materials* (2015).
22. S. R. Pouran, A. A. A. Raman, and W. M. A. W. Daud, Review on the application of modified iron oxides as heterogeneous catalysts in Fenton reactions, *J. Cleaner Production.*, **64** , 24 (2014).
23. M. Chirita, I. Grozescu, L. Taubert, H. Radulescu, and E. Princz, Fe2O3–nanoparticles, physical properties and their photochemical and photoelectrochemical applications, *Chem. Bull.*, **54**, 1 (2009).
24. P. Guardia, A. Labarta, and X. Batlle, Tuning the size, the shape, and the magnetic properties of iron oxide nanoparticles, *The J. Phys. Chem. C*, **115**, 390 (2011).
25. J. Huang, S. Vongehr, S. Tang, H. Lu, X. Meng, Highly catalytic Pd− Ag bimetallic dendrites, *J. Phys. Chem. C*, **114,** 15005 (2010).
26. W. Qin, C. Yang, R. Yi, G. Gao, Hydrothermal synthesis and characterization of single-crystalline *J.Nanomat., **5** ,* 43 (2011).
27. A. Figuerola, R. Di Corato, L. Manna, T. Pellegrino, From iron oxide nanoparticles towards advanced iron-based inorganic materials designed for biomedical applications, *Pharmacol. Res. Commun.*, **62,** 126 (2010).
28. K. Sivula, R. Zboril, F. Le Formal, R. Robert, A. Weidenkaff, J. Tucek, J. Frydrych, M. Gratzel, Photoelectrochemical water splitting with mesoporous hematite prepared by a solution-based colloidal approach, *J. Am. Chem. Soc.*, **132,** 7436 (2010).
29. S. Schwaminger, D. Bauer, P. Fraga-García, F. Wagner, S. Berensmeier, Oxidation of magnetite nanoparticles: impact on surface and crystal properties, *Cryst.Eng.Comm.*, **19,** 246 (2017).

30. M. Nidhin, R. Indumathy, K.J. Sreeram, B.U. Nair, Synthesis of iron oxide nanoparticles of narrow size distribution on polysaccharide templates, *Bull. Mater. Sci.*, **31,** 93 (2008).
31. G. Wang, J. Yang, J. Park, X. Gou, B. Wang, H. Liu, J. Yao, Facile synthesis and characterization of graphene nanosheets, *J. Phys. Chem. C.*, **112,** 8192 (2008).
32. G. Agnelli, D.J. George, A.K. Kakkar, W. Fisher, M.R. Lassen, P. Mismetti, P. Mouret, U. Chaudhari, F. Lawson, A.G. Turpie, Semuloparin for thromboprophylaxis in patients receiving chemotherapy for cancer, *N. Engl. J. Med.*, **366,** 601 (2012).
33. T. Qi, S. Song, Q. Ren, D. Wu, H. Huang, Y. Chen, M. Fan, W. Peng, C. Ren, D. Xie, The Jasmonate-ZIM-domain proteins interact with the WD-Repeat/bHLH/MYB complexes to regulate Jasmonate-mediated anthocyanin accumulation and trichome initiation in Arabidopsis thaliana, *The Plant Cell*, **23,** 1795 (2011).
34. M. Shah, A. Balouch, E. Alveroglu, Sensitive fluorescence detection of Ni 2+ ions using fluorescein functionalized Fe 3 O 4 nanoparticles, *J. Mater. Chem. C*, **6,** 1105 (2018).
35. M. T. Shah, E. Alveroglu, A. Balouch, Pyranine functionalized Fe3O4 nanoparticles for the sensitive fluorescence detection of Cu2+ ions, *J. Alloys Compd.*, **767,** 151 (2018).
36. L. Li, Y. Yang, J. Ding, J. Xue, Synthesis of magnetite nanooctahedra and their magnetic field-induced two-/three-dimensional superstructure, *Chem. Mater.*, **22,** 3183 (2010).
37. Y. T. He, J. Wan, T. Tokunaga, Kinetic stability of hematite nanoparticles: the effect of particle sizes, *J. Nanoparticle Res.*, **10,** 321 (2008).
38. N. M. Khalil, T. C. F. D. Nascimento, D. M. Casa, L. F. Dalmolin, A. C. D. Mattos, I. Hoss, M. A. Romano, and R. M. Mainardes, Pharmacokinetics of curcumin-loaded PLGA and PLGA–PEG blend nanoparticles after oral administration in rats, *Colloids and Surfaces B: Biointerfaces.*, **101,** 353 (2013).
39. C. S. Ciobanu, S. L. Iconaru, E. Gyorgy, M. Radu, M. Costache, A. Dinischiotu, P. L. Coustumer, K. Lafdi, and D. Predoi, Biomedical properties and preparation of iron oxide-dextran nanostructures by MAPLE technique, *Chem. Cent . J .*, **6**, 1 (2012).
40. C. L. Lin, C. F. Lee, and W.Y. Chiu, Preparation and properties of poly (acrylic acid) oligomer stabilized superparamagnetic ferrofluid, *J. Colloid and Interface Sci.*, **291**, 411 (2005).
41. K. Byrappa, A. Subramani, S. Ananda, K.L. Rai, R. Dinesh, M. Yoshimura, Photocatalytic degradation of rhodamine B dye using hydrothermally synthesized ZnO, *Bull. Mater. Sci.*, **29,** 433 (2006).
42. Xu, Renliang, Particle characterization: Light scattering methods, *China Particuology.*, **6**, 271 (2019).
43. M. H. Razali, A. F. M. Noor, and M. Yusoff Hydrothermal Synthesis and Characterization of Cu2+/F–Co-Doped Titanium Dioxide (TiO2) Nanotubes as Photocatalyst for Methyl Orange Degradation, Sci. Adva. Materials, **9,** 1032 (2017).
44. Nguyen, Thi Dung, Ngoc Hoa Phan, Manh Huy Do, and Kim Tham Ngo. "Magnetic Fe_2MO_4 (M: Fe, Mn) activated carbons: fabrication, characterization and heterogeneous Fenton oxidation of methyl orange." *Journal of Hazardous Materials*, **185**, 653 (2011).
45. A. Jahagirdar, M.Z. Ahmed, N. Donappa, H. Nagabhushana, B. Nagabhushana, Photocatalytic degradation of rhodamine B using nanocrystalline α-Fe 2 O 3, *J. Mater. Environ. Sci.*, **5,** 1426 (2014).
46. N. Hariprasad, S. Anju, E. Yesodharan, Sunlight induced removal of Rhodamine B from water through semiconductor photocatalysis: effects of adsorption, reaction conditions and additives, *Research J. Mater. Sci.*, **2320,** 6055 (2013).
47. F. Motahari, M.R. Mozdianfard, M. Salavati-Niasari, Synthesis and adsorption studies of NiO nanoparticles in the presence of H2acacen ligand, for removing Rhodamine B in wastewater treatment, *Process Saf Environ*, **93,** 282 (2015).